ACS APPLIED ENERGY MATERIALS

www.acsaem.org
Article

Synergistic Transition-Metal Coordination within Pyrene- and Phenanthroline-Tethered Conjugated Microporous Polymers for Boosting Hydrogen Evolution Reaction in Alkaline Media

Tapomay Mondal,[#] Mohamed Gamal Mohamed,[#] Muhammed Fasil Puthiyaparambath, Ranjit Thapa, and Shiao-Wei Kuo*

Cite This: ACS Appl. Energy Mater. 2026, 9, 1790−1802
Read Online

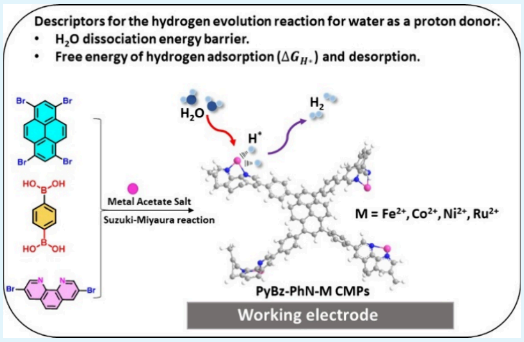

ABSTRACT: Hydrogen (H_2) production via electrochemical water (H_2O) splitting relies heavily on the development of cost-effective and durable electrocatalysts to replace scarce and expensive platinum. Herein, we disclose a rationally conceived and executed synthesis of a pyrene (Py)- and phenanthroline (PhN)- tethered conjugated microporous polymer (CMP), where 1,10-phenanthroline (PhN) ligands (PyBz-PhN CMP) are incorporated through a C−Br/C−B Suzuki−Miyaura cross-coupling strategy. To enhance electrocatalytic activity, transition-metal ions (Fe^{2+}, Co^{2+}, Ni^{2+}, and Ru^{2+}) were coordinated with the PhN sites, affording a series of PyBz-PhN-M CMPs. Comprehensive characterization techniques, including Fourier transform infrared spectroscopy (FTIR), thermogravimetric analysis (TGA), X-ray photoelectron spectroscopy (XPS), ultraviolet photoelectron spectroscopy (UPS), and scanning electron microscopy/energy-dispersive X-ray spectroscopy (SEM-EDS), confirmed successful metal coordination, excellent structural stability, and uniform metal dispersion throughout the framework. Among these catalysts, PyBz-PhN-Ru CMP exhibited the best HER performance, achieving overpotentials of 217 mV at 10 mA cm^{-2} in alkaline media and 180 mV in acidic conditions, alongside a reduced charge-transfer resistance (R_{ct}) of 89 Ω. Combined density functional theory (DFT) calculations and experimental results reveal that modulation of the d-band center and reduced charge-transfer barriers are key to the enhanced catalytic activity. This study demonstrates that phenanthroline-functionalized CMPs serve as versatile and tunable porous platforms for incorporating transition metals, offering a practical approach to creating efficient and low-cost HER catalysts for clean H_2 production.

KEYWORDS: *pyrene, phenanthroline, conjugated microporous polymers, hydrogen evolution reaction, alkaline media, density functional theory*

INTRODUCTION

Hydrogen (H_2) is a globally important chemical widely used in key industrial processes such as petroleum refining and ammonia synthesis; however, its current production predominantly relies on fossil fuels such as natural gas and coal.[1,2] As a promising clean energy carrier, hydrogen has been proposed for applications ranging from powering vehicles and electronic devices to residential energy systems.[3] Therefore, developing cost-effective and sustainable methods for hydrogen production from renewable sources is essential to reduce dependence on fossil fuels and mitigate global CO_2 emissions.[4−6] In recent years, extensive research efforts have focused on generating hydrogen from water through solar-to-hydrogen conversion via photoelectrochemical or electrolysis routes.[7] The HER, a key half-reaction in water splitting, largely governs the overall efficiency of H_2 production. Achieving maximum energy efficiency in water electrolysis requires catalysts that can minimize the additional potential (overpotential) necessary to initiate the HER.[8] Platinum (Pt) is widely regarded as the benchmark electrocatalyst for the HER due to its excellent activity and stability. However, the large-scale deployment of Pt-based catalysts is severely constrained by their high cost and limited availability.[9] To address this challenge, metallic ruthenium (Ru) has emerged as a promising alternative, offering a favorable balance between catalytic performance and cost, along with suitable H_2 adsorption energy.[10] Moreover, transition metal-based compounds derived from earth-abundant elements such as Ni, Co, Fe, and Mo have also demonstrated encouraging HER activity.[11] Various transition-

Received: November 20, 2025
Revised: December 28, 2025
Accepted: January 9, 2026
Published: January 15, 2026

https://doi.org/10.1021/acsaem.5c03684

metal-based materials, including sulfides, nitrides, carbides, phosphides, chalcogenides, and their alloys, have been reported as effective HER electrocatalysts.[12] Nevertheless, the catalytic performance of bulk transition-metal-based materials is often limited by their low specific surface area and insufficient exposure of active sites [Figure 1a].[13] A practical solution to these limitations involves incorporating transition metals into porous frameworks [Figure 1b], which effectively increases the specific surface area and facilitates the uniform dispersion of active sites.[14] The integration of electrochemically active metal centers within porous networks not only enhances intrinsic catalytic activity and selectivity but also ensures efficient metal utilization, thereby reducing overall material cost.[15] Among various porous organic frameworks, such as covalent organic frameworks (COFs), metal–organic frameworks (MOFs), and CMPs have unfolded as highly promising materials for energy storage and electrocatalytic applications.[16−20] This is attributed to their expanded π-conjugated networks, large surface area, structural tunability, low density, controllable band configuration, and superior thermal and chemical durability.[21−30] A key strategy for achieving strong metal–framework interactions and uniform dispersion of active sites within CMPs is the incorporation of electron-donating ligands such as porphyrin,[31,32] bipyridine,[33,34] salen,[35,36] and 1,10-phenanthroline (PhN).[37,38] Coordination of transition metals with these ligands through M–N or M–O bonds can effectively modulate the electronic structure by tuning the d-band center, thereby enhancing electrocatalytic activity.[39] Owing to these advantages, numerous studies have reported the development of metal-coordinated CMP-based catalysts for HER. For example, Das et al. developed Cu(II)- and Ni(II)-grafted porphyrin-pyrene-based CMPs that achieved an overpotential of 532 and 483 mV, respectively, at 10 mA cm^{-2} for the HER.[40] Likewise, Jia et al. synthesized a cobalt-embedded porphyrin-based CMP that reported 360 mV of overpotential to deliver 10 mA cm^{-2}.[41] Despite these advances, most studies have concentrated on porphyrin-based ligands as metal coordination centers. In contrast, other versatile ligands such as 1,10-phenanthroline (PhN) remain largely unexplored for HER applications. Moreover, the influence of different transition-metal coordination environments on the electronic properties of CMPs, an essential factor in determining catalytic performance, has not been systematically investigated.

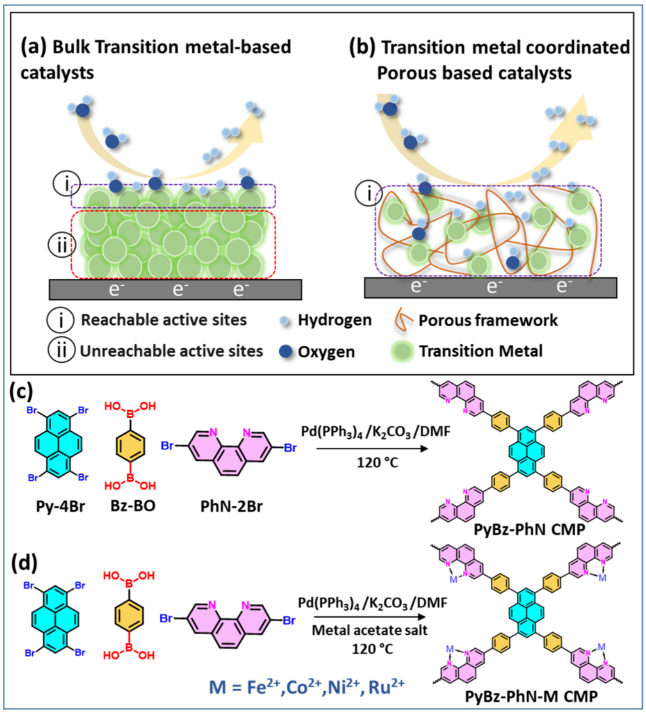

Figure 1. (a) Highlighting the problem in bulk transition metal-based catalysts, which suffer from low active surface area. (b) Approaches to solving the issue by incorporating transition metals into porous frameworks increase surface area and disperse active sites. By leveraging the advantages of CMP, ligands, and transition metals, we propose the metal-coordinated CMP-based catalysts for HER application. (c) Synthesis route of pristine PyBz-PhN CMP and (d) synthesis route of metal-coordinated PyBz-PhN-M CMPs (M = Fe^{2+}, Co^{2+}, Ni^{2+}, and Ru^{2+}).

In this study, we report a simple and scalable approach for synthesizing a pyrene-based CMP incorporating 1,10-phenanthroline (PhN) units as coordinating ligands, designated as PyBz-PhN CMP, via a C–Br/C–B Suzuki–Miyaura cross-coupling reaction. Building on this framework, several metal-coordinated PyBz-PhN CMPs were prepared through coordination with transition-metal salts (Fe^{2+}, Co^{2+}, Ni^{2+}, Ru^{2+}). Comprehensive characterization [including FTIR, TGA, XPS, UPS, SEM, and EDS mapping] confirmed the successful synthesis, structural integrity, uniform metal dispersion, and moderate porosity of the materials. Among the series, PyBz-PhN-Ru CMP exhibited the most outstanding HER performance, requiring an overpotential of only 217 mV to achieve 10 mA cm^{-2} in alkaline medium and 180 mV in acidic conditions. Additionally, an extremely low R_{ct} of 89 Ω was observed at 200 mV overpotential in alkaline conditions, highlighting its excellent electron-transfer kinetics. Ultraviolet photoelectron spectroscopy (UPS) and density functional theory (DFT) calculations further revealed that the superior catalytic activity arises from optimized d-band modulation and reduced energy barriers for charge transfer during hydrogen evolution. This study conclusively demonstrates that electron-active transition metals (Fe^{2+}, Co^{2+}, Ni^{2+}, Ru^{2+}), when coordinated within a 1,10-phenanthroline-functionalized CMP framework, can efficiently promote water reduction reactions. The PyBz-PhN-based CMPs thus represent a versatile and durable platform for the rational design of next-generation HER catalysts, advancing sustainable and cost-effective hydrogen production technologies.

■ EXPERIMENTAL SECTION

Materials

Potassium carbonate (K_2CO_3, 99.9%), pyridine, pyrene (Py, 98%), 1-chlorobutane, 1,10-phenanthroline (PhN), nitrobenzene ($C_6H_5NO_2$), disulfur dichloride (S_2Cl_2), iron(II) acetate [$Fe(CH_3COO)_2$], bromine solution (Br_2), cobalt(II) acetate [$Co(CH_3COO)_2$], nickel(III) acetate [$Ni(CH_3COO)_2$], ruthenium(II) acetate [$Ru(CH_3COO)_2$], pyridine, $Pd(PPh_3)_4$, methanol (MeOH) were purchased from Sigma-Aldrich and Acros. 1,4-Benzenediboronic acid [Bz-BO, 95%], acetone, and tetrahydrofuran (THF) were obtained from Alfa Aesar. The compound 1,3,6,8-tetrabromopyrene (Py-4Br) was obtained using the synthetic route developed in our previous research.[42−46]

Synthesis of 3,8-Dibromo-1,10-phenanthroline (PhN-2Br)

In a 1 L three-neck flask, 1-chlorobutane (142 mL), PhN (3.55 g, 19.74 mmol), pyridine (5.33 mL), and S_2Cl_2 (5.7 mL) were heated at 100 °C. Br_2 (4 mL) was then added dropwise, and the system was subjected to reflux for 12 h. Then, the reaction was quenched with

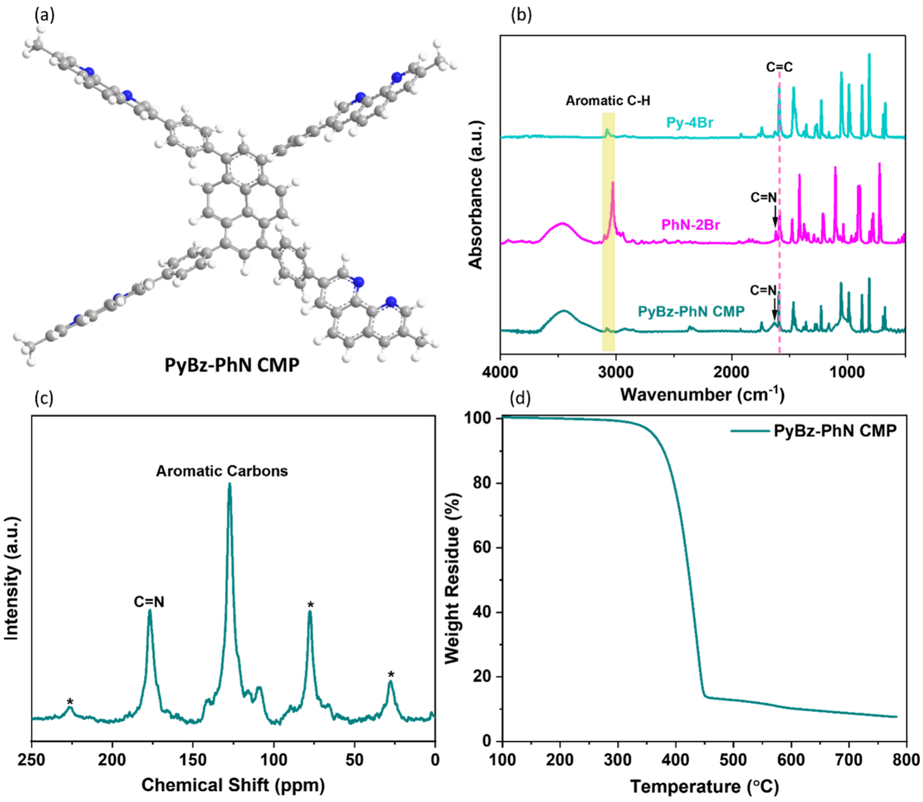

Figure 2. (a) 3D structure image of PyBz-PhN CMP, (b) FTIR spectrum of Py-4Br, PhN-2Br, and PyBz-PhN CMP. (c) Solid-state ^{13}C NMR and (d) TGA thermogram of PyBz-PhN CMP.

saturated NaOH (aq, 50 mL). the crude solid product was washed with water and extracted with CH_2Cl_2 to afford a pure white product (1.8 g, 52%). ^{1}H NMR (DMSO-d_6, ppm): 9.16 (2H), 8.86 (2H), 8.03 (2H). ^{13}C NMR (DMSO-d_6, ppm): 150.75, 143.64, 137.94, 129.73, 126.86, 119.47.

Synthesis of PyBz-PhN CMP and PyBz-PhN-M CMPs

In a 25 mL Pyrex tube, a mixture of Py-4Br (0.33 g, 0.64 mmol), Bz-BO (0.32 g, 1.93 mmol), PhN-2Br (0.22 g, 0.64 mmol), and $Pd(PPh_3)_4$ (0. 04 g, 0.032 mmol) was added 20 mL of DMF and 5 mL of 2 M K_2CO_3. The mixture was purged of gases by performing three freeze−pump−thaw cycles under nitrogen. Then, the reaction mixture was heated up to 110 °C for 5 days. The obtained solid was separated by filtration, thoroughly rinsed with THF, Water, DMF, MeOH, and acetone to produce PyBz-PhN CMP as a yellow powder [0.26 g, 79%]. An analogous synthetic route to that of PyBz-PhN CMP was adopted for preparing PyBz-PhN-M CMPs, a mixture was prepared by combining $Ru(CH_3COO)_2$ (0.64 mmol), $Fe(CH_3COO)_2$ (0.64 mmol), $Co(CH_3COO)_2$ (0.64 mmol), or $Ni(CH_3COO)_2$ (0.64 mmol) with Py-4Br (0.33 g, 0.64 mmol), Bz-2BO (0.32 g, 1.93 mmol), PhN-2Br (0.22 g, 0.64 mmol), and $Pd(PPh_3)_4$ (0.04g, 0.032 mmol) to produce a dark brown powder for PyBz-PhN-Fe CMP, PyBz-PhN-Co CMP, PyBz-PhN-Ni CMP, and a dark blackish brown for PyBz-PhN-Ru CMP; respectively.

RESULTS AND DISCUSSION

Synthesis and Characterization of PyBz-PhN CMP and PyBz-PhN-M CMPs

The presence of N,N′-chelating sites in 1,10-phenanthroline (PhN) makes it an ideal monomer for coordinating metal centers, enabling the formation of robust coordination complexes with highly active catalytic sites for enhanced electrocatalytic performance. The precursor PhN-2Br, which employed a ligand capable of forming coordination bonds with metal ions in this study, was synthesized via the reaction of PhN with S_2Cl_2 and Br_2 in the presence of pyridine, yielding a white solid [Scheme S1]. The chemical structure of PhN-2Br was confirmed by ^{1}H and ^{13}C NMR analyses. The ^{1}H NMR spectrum exhibited three characteristic aromatic proton signals at 9.16, 8.86, and 8.03 ppm, corresponding to the protons in the PhN moiety [Figure S1]. Additionally, the ^{13}C NMR spectrum displayed aromatic carbon resonances in the range of 150.75−119.47 ppm, further verifying the formation and structure of the desired compound [Figure S2]. To synthesize the PyBz-PhN CMP, Py-4Br, Bz-BO, and PhN-2Br were used as the main building blocks. These monomers underwent a Suzuki−Miyaura cross-coupling reaction in a DMF/2 M K_2CO_3 solvent mixture under continuous stirring and steady heating for 3 days, yielding PyBz-PhN CMP as a yellow powder [Figure 1c]. Figure 2a displays the three-dimensional (3D) structural model of PyBz-PhN CMP. The structural evolution of PyBz-PhN CMP from its monomeric precursors, Py-4Br and PhN-2Br, was confirmed by Fourier-transform infrared (FT-IR) spectroscopy. As shown in Figure 2b, the absorption peaks observed at 3077−3067 cm^{-1} correspond to the sp^2 (aromatic) C−H stretching vibrations. A C═C stretching band appears at 1600−1586 cm^{-1} for Py-4Br, PhN-2Br, and PyBz-PhN CMP, while both PhN-2Br and PyBz-PhN CMP exhibit a C═N absorption peak at 1632 cm^{-1}. The disappearance of the characteristic C−Br absorption bands in the FT-IR spectrum of PyBz-PhN CMP further confirms the successful incorporation of pyrene and PhN units into the polymer framework. Solid-state ^{13}C NMR spectroscopy [Figure 2c] revealed broad resonances between 105 and 146 ppm, attributable to aromatic carbons of the pyrene, benzene, and phenanthroline moieties. A distinct resonance at

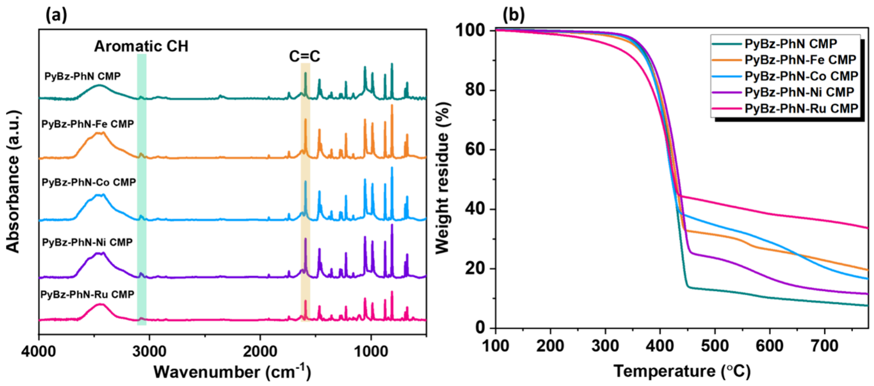

Figure 3. (a) FTIR spectra and (b) TGA traces of PyBz-PhN CMP, and PyBz-PhN-M (M = Fe^{2+}, Co^{2+}, Ni^{2+}, and Ru^{2+}) CMP.

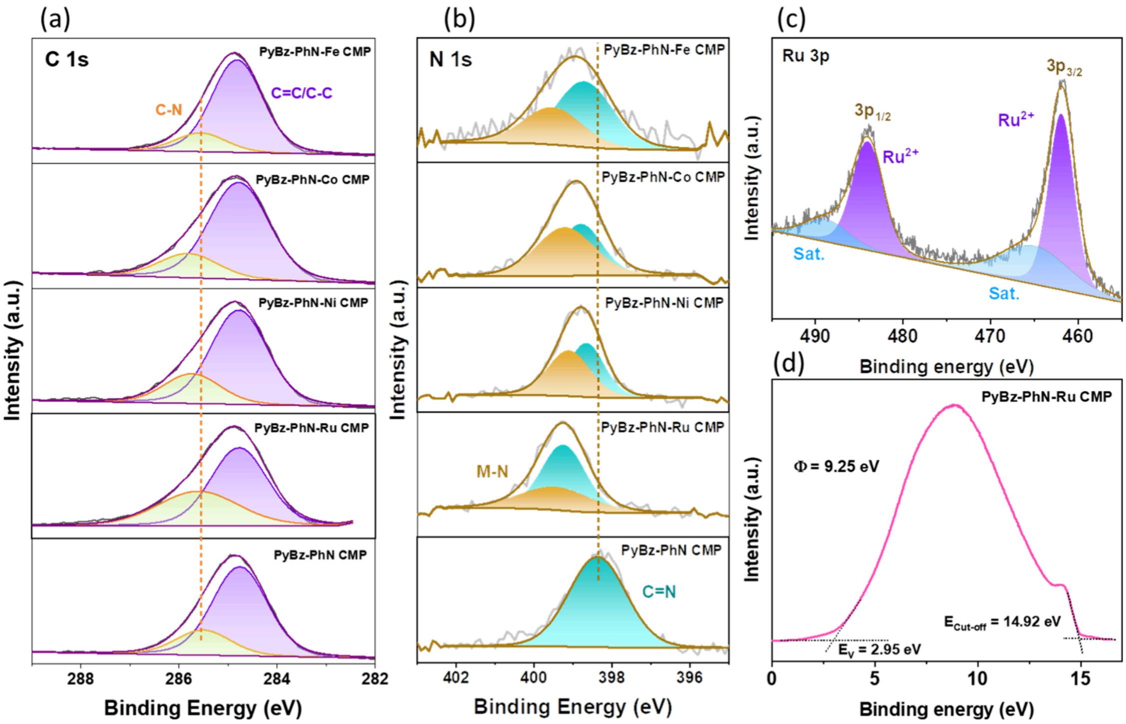

Figure 4. High-resolution spectra of (a) C 1s, and (b) N 1s of PyBz-PhN and PyBz-PhN-M CMPs catalysts, (c) high-resolution spectra of Ru 3p, and (d) ultraviolet photoelectron spectroscopy data of PyBz-PhN-Ru CMP.

176 ppm corresponds to the C═N carbons of the phenanthroline ligands, confirming the formation of PyBz-PhN CMP. Thermogravimetric analysis (TGA) [Figure 2d] demonstrated remarkable thermal stability, with decomposition temperatures (T_5% and T_{10}%) of 362 and 376 °C, respectively, and a char yield of 8 wt % under N_2, indicating excellent structural integrity.

A family of metal-coordinated PyBz-PhN CMPs frameworks (PyBz-PhN-M, where M = Fe^{2+}, Co^{2+}, Ni^{2+}, Ru^{2+}) was subsequently synthesized via a one-pot Suzuki−Miyaura coupling in DMF/2 M K_2CO_3 containing $Fe(CH_3COO)_2$, $Co(CH_3COO)_2$, $Ni(CH_3COO)_2$ and $Ru(CH_3COO)_2$ salts. The reaction mixture was stirred continuously for 5 days to yield the corresponding PyBz-PhN-M CMPs. Due to their intrinsic insolubility in both polar and nonpolar solvents, the resulting products were isolated as solid powders [Figure 1d]. FT-IR spectra [Figure 3a] of all PyBz-PhN-M CMPs samples displayed distinct bands at 3000−3100 and 1600−1586 cm^{-1}, signifying the vibrational modes of aromatic C−H and C═C groups. Notably, a new absorption band at approximately 1467 cm^{-1}, assigned to C═N vibrations linked to M−N coordination, confirmed the successful integration of Ru, Fe, Co, and Ni ions into the polymeric network.[47] TGA analysis [Figure 3b] demonstrated that all PyBz-PhN-M CMPs possess outstanding thermal stability, with T_{10}% values of 377 °C (Fe), 375 °C (Co), 383 °C (Ni) and 355 °C (Ru), The respective char yields were 19 wt % (Fe), 17 wt % (Co), 12 wt % (Ni), and 33 wt % (Ru), reflecting their excellent structural robustness at elevated temperatures.

To elucidate the chemical environment of the C, N, and metal centers, X-ray photoelectron spectroscopy (XPS) was performed. XPS survey spectra (Figure S3) confirmed the presence of C and N in all samples. In addition, distinct metal-related peaks for Ru, Fe, Co, and Ni were clearly detected in the corresponding PyBz-PhN-M CMPs spectra, verifying successful incorporation of each metal into the respective framework. The presence of a minor oxygen peak was attributed to moisture adsorption from the environment.[48]

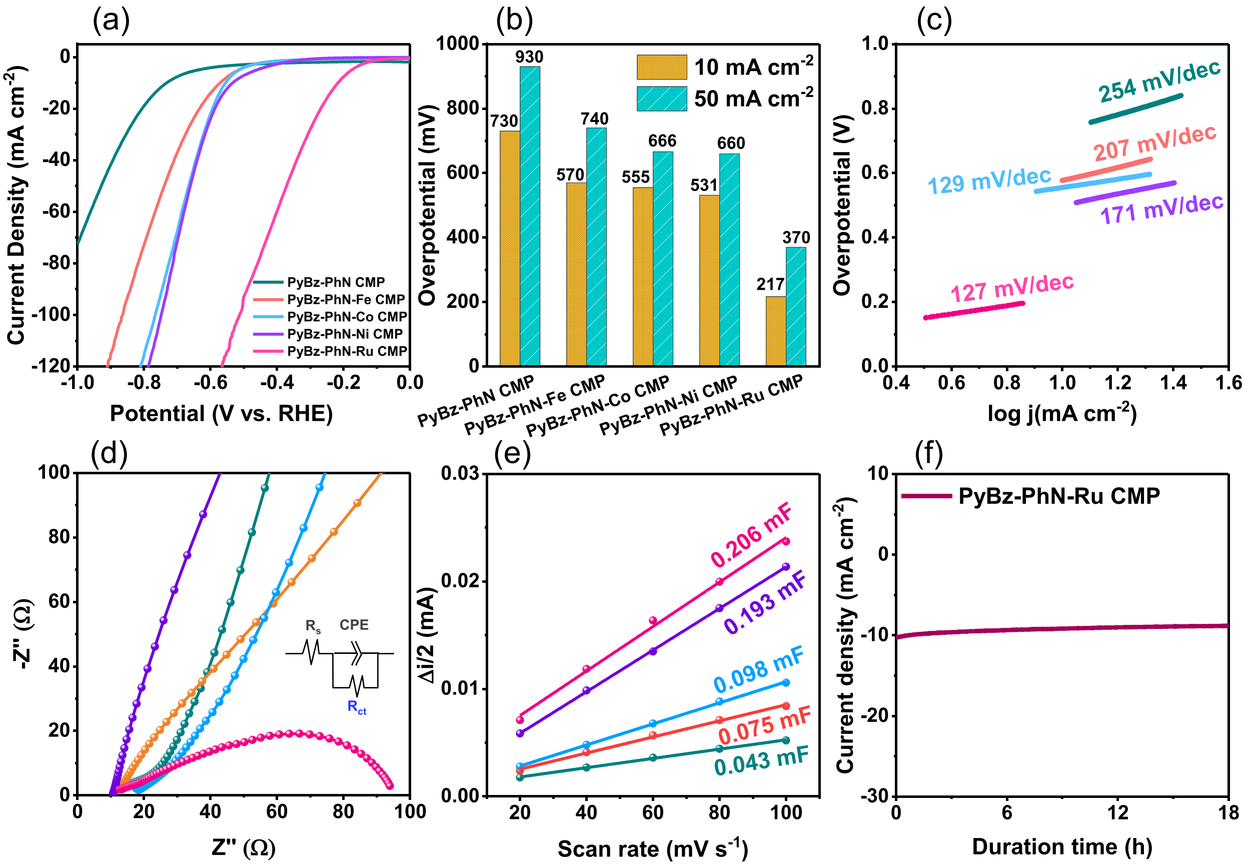

Figure 5. (a) HER polarization curves of all prepared PyBz-PhN and PyBz-PhN-M CMPs catalysts in 1 M KOH electrolytes, (b) comparison bar charts of overpotentials at different current densities of PyBz-PhN and PyBz-PhN-M CMPs catalysts, (c) corresponding Tafel slopes, (d) Nyquist plots (inset: the equivalent circuit), (e) C_{dl}, and (f) chronoamperometry graph of PyBz-PhN-Ru CMP [recorded in 1 M KOH].

The high-resolution C 1s spectrum of PyBz-PhN CMP [Figure 4a] displayed peaks at 284.8 and 286.0 eV, corresponding to C−C/C═C and C═N bonds, respectively. Upon metal coordination, the C═N peak shifted to higher binding energy, indicating metal-to-ligand charge transfer (MLCT) between the transition-metal centers and phenanthroline ligands.[49,50] The N 1s spectrum of PyBz-PhN CMP [Figure 4b] showed a single peak characteristic of C═N in the phenanthroline unit, which acts as a chelating site for metal coordination.[50−53] In PyBz-PhN-M CMPs, the N 1s peak shifted to higher binding energy and exhibited an additional component at 399.2 eV, confirming M−N bond formation. The calculated N 1s peak area percentages of the PyBz-PhN-M CMPs, derived from N 1s XPS deconvolution, are listed in Table S2. High-resolution XPS spectra of the metal centers further verified their oxidation states [Figures 4c and S4]: Ru 3p (461.9 and 484.1 eV, Ru^{2+}),[54] Fe 2p (710.9 eV/723.1 eV for Fe^{2+} and 713.0 eV/725.3 eV for Fe^{3+}),[55,56] Co 2p (781.3 and 797.5 eV, Co^{2+}),[57] and Ni 2p (855.4 and 872.9 eV, Ni^{2+}).[54] These findings confirm the successful coordination of the respective metal ions within the PyBz-PhN CMP polymer framework. To further understand the surface electronic properties, ultraviolet photoemission spectroscopy (UPS) was used to analyze the electron modulation behavior of the catalysts. The work function (Φ), which estimates the minimum energy an electron must possess to escape from the Fermi level to the vacuum, was evaluated using eq 1:[58]

$$\Phi = h\nu - w \tag{1}$$

where $h\nu$ is the photon energy (21.22 eV for He I radiation) and w is the spectral width determined by the difference between the valence band maximum (E_v) and secondary electron cutoff (E_{cutoff}). As shown in Figure 4d and Figure S5(a−d), PyBz-PhN-Ru CMP exhibited the lowest work function (9.25 eV) compared to PyBz-PhN-Fe CMP (9.44 eV), PyBz-PhN-Co CMP (9.36 eV), PyBz-PhN-Ni CMP (9.31 eV), and pristine PyBz-PhN CMP(9.74 eV), indicating a reduced energy barrier for electron transfer during redox processes.

Porosity and surface area were examined using N_2 adsorption−desorption isotherms at 77 K [Figure S6 and Table S1]. The Brunauer−Emmett−Teller (BET) surface areas were determined as 32.5, 3.02, 12.6, 5.54, and 8.42 m^2 g^{-1} for PyBz-PhN, PyBz-PhN-Fe, PyBz-PhN-Co, PyBz-PhN-Ni, and PyBz-PhN-Ru CMPs. The nonlocal density functional theory (NLDFT) pore size distribution revealed an average pore diameter of 2.67 nm for PyBz-PhN CMP, while metal coordination led to reduced pore sizes, 2.23 nm (Fe), 1.96 nm (Co), 1.87 nm (Ni), and 1.78 nm (Ru), attributed to partial pore occupation by metal centers, thereby reducing overall porosity.[59] Morphological analysis via field-emission scanning electron microscopy (FESEM) revealed that pristine PyBz-PhN CMP exhibits a rod-like morphology, whereas its metal-coordinated derivatives (PyBz-PhN-M CMPs) display aggregated spherical particles intertwined with rod-like structures [Figures S7−S10]. In particular, PyBz-PhN-Ru CMP exhibited a higher degree of spherical aggregation [Figure S11], likely enhancing active site exposure for HER. Transmission electron microscopy (TEM) images confirmed a layered stacking structure and amorphous character in all synthesized PyBz-PhN and PyBz-PhN-M CMPs [Figures S12−S16], while TEM-EDS elemental mapping demonstrated uniform distributions of C and N in PyBz-PhN, and homogeneous dispersion of Ru, Fe, Co, and Ni in their respective metal-coordinated frameworks, verifying successful and uniform metal incorporation [Figures S17−S21]. Moreover, the metal content of PyBz-PhN-Fe, PyBz-PhN-Co, PyBz-PhN-Ni, and PyBz-PhN-Ru CMPs is determined by the inductively coupled plasma optical emission spectroscopy (ICP-OES), and the metal content of 10.93, 9.39, 9.81, and 11.38 wt % of Fe, Co, Ni, and Ru, respectively are present in their respective metal-coordinated CMP network.

Electrocatalytic Activity of PyBz-PhN CMP and PyBz-PhN-M CMPs toward the Hydrogen Evolution Reaction (HER) under Both Alkaline and Acidic Conditions

To assess the electrocatalytic activities of the synthesized PyBz-PhN CMP and PyBz-PhN-M CMPs, hydrogen evolution reaction (HER) measurements were carried out implementing a standard three-electrode system in 1 M KOH. While Hg/HgO and Pt wire behaved as the reference and counter electrodes, respectively. As illustrated in Figure 5a,b, the linear sweep voltammetry (LSV) profiles reveal that the pristine PyBz-PhN CMP catalyst exhibits the lowest HER activity, requiring large overpotentials of 730 and 930 mV to achieve current densities of 10 and 50 mA cm^{-2} (η_{10} and η_{50}, respectively) in alkaline medium. In contrast, the metal-coordinated PyBz-PhN CMPs catalysts displayed markedly improved activity, delivering higher current densities at significantly lower overpotentials. The overpotentials at η_{10}, and η_{50} follow the order: PyBz-PhN-Ru CMP (217, 370 mV) > PyBz-PhN-Ni CMP (531, 660 mV) > PyBz-PhN-Co CMP (555, 666 mV) > PyBz-PhN-Fe CMP(570, 740 mV). The enhanced HER performance of the metal-coordinated catalysts clearly demonstrates the beneficial role of metal incorporation in facilitating charge transfer and lowering the energy barrier for H_2 evolution.[60] By comparing the LSV data of Pt/C, the PyBz-PhN-Ru CMP needed 177 mV more overpotential to deliver 10 mA cm^{-2} current density than that of Pt/C (η_{10} = 40 mV) [Figure S22]. Notably, PyBz-PhN-Ru CMP exhibits the best catalytic activity among all metal-coordinated synthesized samples, requiring the smallest overpotential (513 mV) to reach a large current density of 100 mA cm^{-2} [Figure S23]. The Tafel slope, a key descriptor of HER catalytic kinetics, was obtained from the linear region of the Tafel plots, which were derived from the corresponding LSV polarization curves. A lower Tafel slope indicates more favorable HER kinetics, reflecting a steeper rise in catalytic current with smaller overpotential increments. As shown in Figure 5c, the Tafel slopes are 127, 207, 129, 171, and 254 mV dec^{-1} for PyBz-PhN-Ru, PyBz-PhN-Fe, PyBz-PhN-Co, PyBz-PhN-Ni, and pristine PyBz-PhN CMP, respectively. Among all catalysts, PyBz-PhN-Ru CMP exhibits the lowest Tafel slope, demonstrating the fastest reaction kinetics for HER. The Tafel slope values of all CMP-based catalysts fall within the regime characteristic of alkaline HER governed by water dissociation, indicating that the Volmer step (H_2O dissociation and initial proton discharge) is the rate-determining step (r.d.s.). Importantly, the significantly reduced Tafel slope of PyBz-PhN-Ru CMP compared to PyBz-PhN-Fe, PyBz-PhN-Co, and PyBz-PhN-Ni CMPs confirms that Ru coordination effectively promotes the Volmer step by accelerating proton discharge and enhancing electron-transfer efficiency. This suggests that Ru incorporation lowers the kinetic barrier associated with water dissociation and improves interfacial charge transport, leading to more efficient catalytic turnover during HER.[61] This synergistic effect accounts for the enhanced HER kinetics and superior overall catalytic activity of PyBz-PhN-Ru CMP. Electrochemical impedance spectroscopy (EIS) was performed at an overpotential of 200 mV to further assess the charge transfer characteristics of the catalysts [Figures S24 and 5d]. The Nyquist plots reveal that PyBz-PhN-Ru CMP exhibits the smallest semicircular diameter in the low-frequency region, indicating a lower charge transfer resistance (R_{ct}). By fitting the Nyquist plot with the equivalent circuit model shown in the inset of Figure 5d, the R_{ct} value for PyBz-PhN-Ru CMP was determined to be 89 Ω. This remarkably low R_{ct} confirms that Ru coordination effectively enhances electron transport across the electrode−electrolyte interface, thereby facilitating faster charge transfer and promoting superior HER kinetics.[62] Table S3 Summarized R_{ct} values of all synthesized PyBz-PhN CMP and PyBz-PhN-M CMPs electrocatalysts at an overpotential of 200 mV in 1 M KOH electrolyte. The exchange current density (j_o) serves as a fundamental parameter for characterizing the intrinsic kinetic activity of electrocatalysts at equilibrium. It quantifies the bidirectional charge (electron) transfer rate across the electrode−electrolyte interface under equilibrium conditions. Typically, j_o is determined using the Tafel extrapolation method, wherein the linear portion of the Tafel plot is extrapolated to zero overpotential. PyBz-PhN-Ru CMP exhibits an exceptional j_o value of 209 mA cm^{-2}, which is significantly higher than those of PyBz-PhN-Fe CMP (17 mA cm^{-2}), PyBz-PhN-Co CMP (0.49 mA cm^{-2}), PyBz-PhN-Ni CMP (7.49 mA cm^{-2}), and the pristine PyBz-PhN CMP (13.3 mA cm^{-2}). This remarkable enhancement clearly demonstrates that Ru coordination markedly accelerates the charge transfer process at the electrode−electrolyte interface, thereby endowing PyBz-PhN-Ru CMP with the highest intrinsic catalytic activity among the investigated materials. Overall, PyBz-PhN-Ru outperforms most previously reported CMP-, COF-, and POP-based catalysts (Table S4), highlighting its strong potential as an efficient and robust electrocatalyst for alkaline HER applications. The improved interfacial conductivity of PyBz-PhN-Ru CMP is crucial to its outstanding electrocatalytic performance. The enhanced electrocatalytic performance of the catalysts can be attributed to the increased electrochemically accessible surface area (ECSA) and the abundance of inherent active sites. To assess these factors, the double-layer capacitance (C_{dl}) was extracted based on CV measurements conducted at various scan rates in the nonfaradaic region. The corresponding CV curves for all catalysts are presented in Figure S25.

As shown in Figure 5e, the PyBz-PhN-Ru CMP catalyst exhibits the highest C_{dl} value of 0.206 mF, followed by PyBz-PhN-Ni CMP (0.193 mF), PyBz-PhN-Co CMP (0.098 mF), PyBz-PhN-Fe CMP (0.075 mF), and PyBz-PhN CMP (0.043 mF). The higher C_{dl} value of PyBz-PhN-Ru suggests a substantially larger electrochemically active surface area, which enhances the availability of catalytic sites for the H_2 evolution reaction. As depicted in Figure 5f, PyBz-PhN-Ru CMP retained approximately 86% of its initial current density after 18 h of continuous operation, demonstrating excellent steady-state catalytic stability. Furthermore, the HER polarization curves recorded before and after 2000 continuous CV

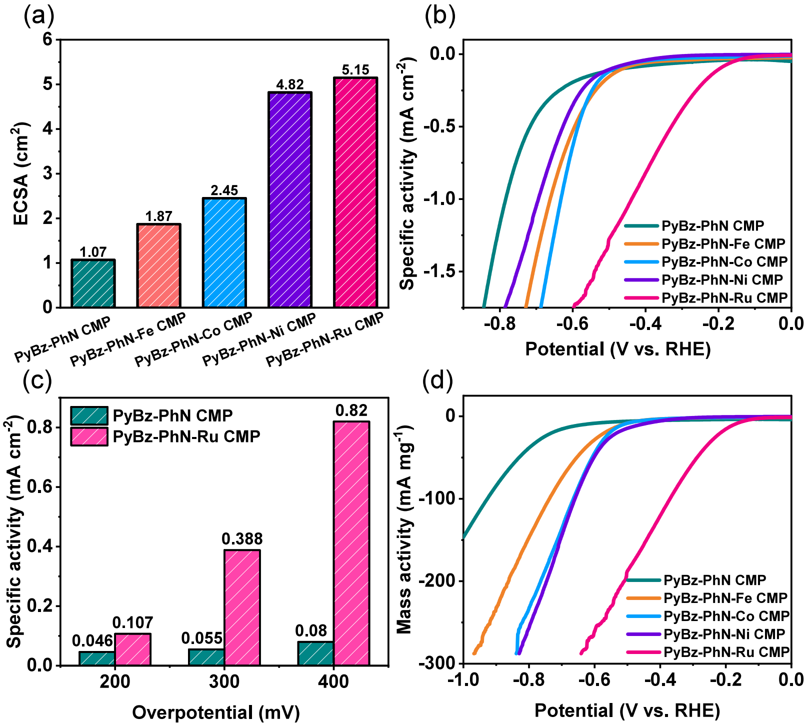

Figure 6. (a) Summarized electrochemical surface area (ECSA) values, (b) calculated specific activity of pristine PyBz-PhN CMP and PyBz-PhN-M CMPs (M = Fe^{2+}, Co^{2+}, Ni^{2+}, Ru^{2}) across a range of overpotentials in 1 M KOH, (c) comparison of specific activity for Pristine PyBz-PhN CMP and PyBz-PhN-Ru CMP at overpotentials of 200, 300, and 400 mV, and (d) Mass activity comparison between pristine PyBz-PhN CMP and PyBz-PhN-M CMPs (M = Fe^{2+}, Co^{2+}, Ni^{2+}, Ru^{2+}) across a range of overpotentials.

cycles [Figure S27] exhibited negligible loss in cathodic current, confirming the superior dynamic stability and robust structural integrity of the PyBz-PhN-Ru CMP catalyst under prolonged electrochemical conditions. Moreover, the PyBz-PhN-Ru CMP maintained approximately 70% retention of initial current density even after prolonged 50 h of chronoamperometric testing, further confirming its noticeable electrochemical stability [Figure S28]. Additionally, SEM images further reveal that the overall porous architecture and surface morphology of PyBz-PhN-Ru CMP are largely retained following prolonged HER operation, demonstrating the material's structural integrity [Figure S29]. Moreover, chronoamperometric tests of PyBz-PhN CMP and its Fe-, Co-, and Ni-coordinated derivatives were performed in 1 M KOH. As shown in Figure S30, the PyBz-PhN CMP demonstrates poor stability for prolonged HER operation. In contrast, the PyBz-PhN-M CMPs (M = Fe^{2+}, Co^{2+}, Ni^{2+}) maintains nearly constant current densities over 18 h, confirming their robust operational stability toward HER. Furthermore, the ECSA values, which are calculated from the respective C_{dl} data (detail is provided in Supporting Information), are 5.15, 1.87, 2.45, 4.82, and 1.07 cm^2 for PyBz-PhN-Ru, PyBz-PhN-Fe, PyBz-PhN-Co, PyBz-PhN-Ni, and PyBz-PhN CMPs, respectively [Figure 6a]. These findings confirm that the PyBz-PhN-Ru CMP holds the largest number of accessible catalytic sites, which play a pivotal role in its superior HER performance by facilitating efficient electron and proton transfer during the reaction process. In addition to the C_{dl} and ECSA values, other critical parameters, such as specific activity, mass activity, and turnover frequency (TOF), were evaluated to gain a deeper understanding of the HER performance. The specific activity was obtained by normalizing the LSV curves with respect to the ECSA of each catalyst, thereby reflecting the intrinsic catalytic activity independent of surface area effects. As reported in Figure 6b, PyBz-PhN-Ru CMP shows a substantially higher specific activity across a wide potential range compared to the pristine PyBz-PhN and its metal-coordinated counterparts PyBz-PhN-M (M = Fe^{2+}, Co^{2+}, Ni^{2+}).

Specifically, at overpotentials of 200, 300, and 400 mV, PyBz-PhN-Ru CMP demonstrates approximately 2.3, 7.0, and 10.2 fold higher specific activity, respectively, than the pristine PyBz-PhN CMP catalyst [Figure 6c]. Furthermore, the mass activity, derived by normalizing the polarization curves to the mass of the loaded catalyst, also highlights the superior performance of PyBz-PhN-Ru CMP. As depicted in Figure 6d, PyBz-PhN-Ru achieves a mass activity exceeding 100 mA mg^{-1} at an overpotential of 370 mV, whereas the pristine PyBz-PhN CMP and PyBz-PhN-M (M = Fe^{2+}, Co^{2+}, Ni^{2+}) catalysts exhibit mass activities below 6 mA mg^{-1} under the same conditions. Notably, PyBz-PhN-M catalysts (M = Fe^{2+}, Co^{2+}, Ni^{2+}) still outperform the pristine PyBz-PhN CMP in the higher overpotential region, confirming the beneficial role of metal coordination. To further assess the intrinsic catalytic efficiency, the TOF values were calculated under alkaline conditions, as described in the Supporting Information. As shown in Figure S26, PyBz-PhN-Ru CMP exhibits an impressive TOF of 65.2 s^{-1} at 450 mV, far exceeding those of the other synthesized catalysts. Overall, the outstanding electrocatalytic performance of PyBz-PhN-Ru CMP can be attributed to its combination of high specific and mass activities, low charge-transfer resistance, and superior intrinsic reaction kinetics (high TOF). These results underscore the effectiveness of Ru coordination in enhancing the catalytic properties of CMP-based frameworks, making PyBz-PhN-Ru CMP a highly active and cost-efficient electrocatalyst for the

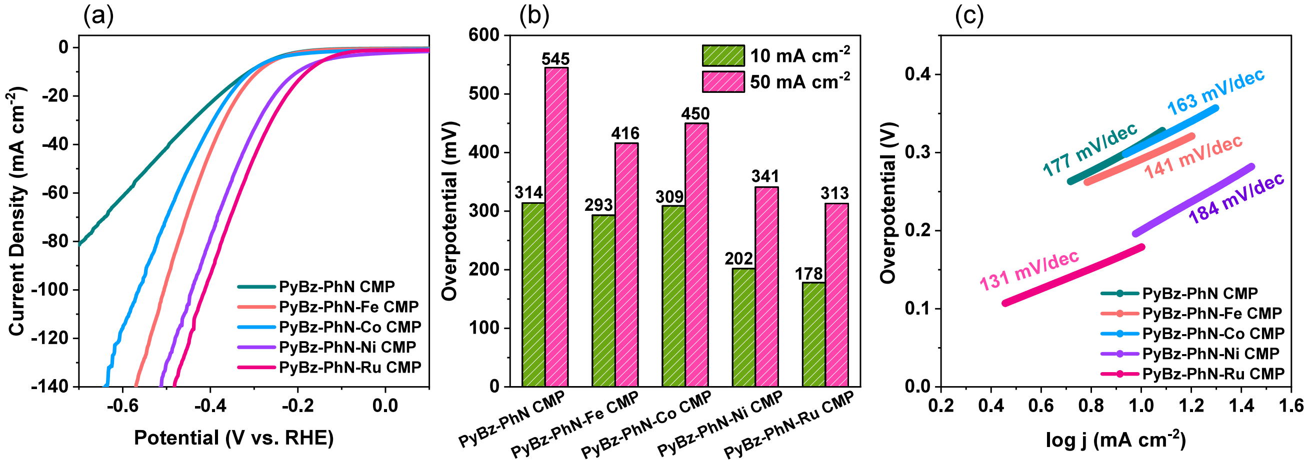

Figure 7. (a) Polarization characteristics of HER and (b) bar representations of overpotentials at 10 and 50 mA cm^{-2} and (c) corresponding Tafel slopes of all prepared PyBz-PhN CMP and PyBz-PhN-M CMPs (M = Fe^{2+}, Co^{2+}, Ni^{2+}, and Ru^{2+}) catalysts in 0.5 M H_2SO_4 electrolyte.

H_2 evolution reaction. In addition to its outstanding HER activity, long-term operational stability is a critical parameter for evaluating the overall catalytic performance. The durability of the PyBz-PhN-Ru CMP catalyst was examined using chronoamperometric measurements at a fixed potential of −0.220 V vs RHE, corresponding to a current density of 10 mA cm^{-2}. To further evaluate the catalytic versatility, the HER activity of the synthesized materials was also investigated in an acidic electrolyte (0.5 M H_2SO_4). The corresponding LSV profiles of all catalysts are shown in Figure 7a. The metal-coordinated catalysts (PyBz-PhN-Ru, PyBz-PhN-Fe, PyBz-PhN-Co, and PyBz-PhN-Ni CMPs) exhibit significantly lower overpotentials compared to the pristine PyBz-PhN CMP, indicating enhanced proton reduction capability. Specifically, PyBz-PhN-Ru CMP requires only 178 mV to achieve a current density of 10 mA cm^{-2} [Figure 7b], outperforming its counterparts PyBz-PhN-Fe CMP (293 mV), PyBz-PhN-Co CMP (309 mV), and PyBz-PhN-Ni CMP (202 mV). Remarkably, even the pristine PyBz-PhN CMP exhibits a relatively low overpotential of 314 mV at 10 mA cm^{-2}, surpassing many previously reported metal-free electrocatalysts [Table S3]. Moreover, at a higher current density of 100 mA cm^{-2}, the PyBz-PhN-Ru CMP required less overpotential of 413 mV [Figure S31]. As illustrated in Figure 7c, the corresponding Tafel slopes further corroborate the superior catalytic kinetics of PyBz-PhN-Ru CMP, which records a slope of 131 mV dec^{-1}, the smallest among all tested catalysts. In comparison, the Tafel slopes for PyBz-PhN-Fe, PyBz-PhN-Co, PyBz-PhN-Ni, and pristine PyBz-PhN CMPs are 141, 163, 184, and 177 mV dec^{-1}, respectively. These findings collectively demonstrate that PyBz-PhN-Ru CMP not only delivers exceptional HER performance in alkaline media but also maintains excellent catalytic efficiency and stability under acidic conditions, underscoring its potential as a robust and versatile electrocatalyst for H_2 evolution.

Exploring the Intrinsic Electrochemical Mechanism of PyBz-PhN CMP and PyBz-PhN-M CMPs for HER

DFT calculations were carried out to elucidate the underlying hydrogen evolution reaction (HER) mechanism of the catalysts in an alkaline medium. Atomic models of the pristine PyBz-PhN CMP and PyBz-PhN-M CMPs (M = Fe^{2+}, Co^{2+}, Ni^{2+}, and Ru^{2+}), were constructed and fully optimized, as depicted in Figures 8a,b, respectively. The calculated binding energies of the PyBz-PhN-M systems, obtained using eq S3, were all negative, confirming that metal incorporation into the CMP framework is thermodynamically favorable. The corresponding binding energy values are provided in Figure S32. Bader charge analysis reveals that, upon metal coordination, electron transfer occurs from the metal ion centers (M) to the CMP framework, following the order: Ru (0.30 e$^-$) < Ni (0.40 e$^-$) < Co (0.43 e$^-$) < Fe (0.46 e$^-$). This gradual increase in electron depletion on the metal centers suggests that the coordination of metal atoms effectively modulates the electronic structure of the CMP, thereby enhancing the intrinsic catalytic activity toward HER by facilitating charge redistribution and improving the adsorption−desorption kinetics of hydrogen intermediates. For alkaline HER, the dissociation of H_2O is a pivotal step, as water serves as the primary proton source in such media, commonly referred to as the Volmer step.[63,64] To prove this process, the adsorption energy of H_2O molecules was first calculated, and the results are shown in Figure 8c. The pristine PyBz-PhN CMP exhibits weak physisorption of H_2O with an adsorption energy of −0.16 eV, whereas the metal-coordinated PyBz-PhN-M CMPs display strong chemisorption of H_2O molecules. The calculated H_2O dissociation barriers, presented in Figure 8d, reveal that pristine PyBz-PhN CMP possesses the highest barrier (1.09 eV), indicating sluggish H−OH bond cleavage and limited formation of H* intermediates, thus accounting for its poor HER kinetics under alkaline conditions. In contrast, the PyBz-PhN-M CMPs catalysts exhibit substantially reduced dissociation barriers of 0.34, 0.24, 0.22, and 0.17 eV for Fe, Co, Ni, and Ru, respectively. Among these, PyBz-PhN-Ru CMP demonstrates the lowest energy barrier, signifying its superior ability to facilitate water dissociation and hydrogen generation. Additionally, the free energy of hydrogen adsorption (ΔG_{H*}) was calculated to assess the thermodynamics of hydrogen intermediate formation.

The DFT results show that PyBz-PhN-Ru CMP possesses the smallest ΔG_{H*}, indicating optimal hydrogen adsorption−desorption balance and enhanced catalytic efficiency. Combining insights from both the H_2O dissociation and hydrogen adsorption steps, PyBz-PhN-Ru clearly offers the most favorable energetics for alkaline HER.[65] Consequently, the predicted activity trend follows the order: PyBz-PhN-Ru CMP > PyBz-PhN-Ni CMP > PyBz-PhN-Co CMP > PyBz-PhN-Fe

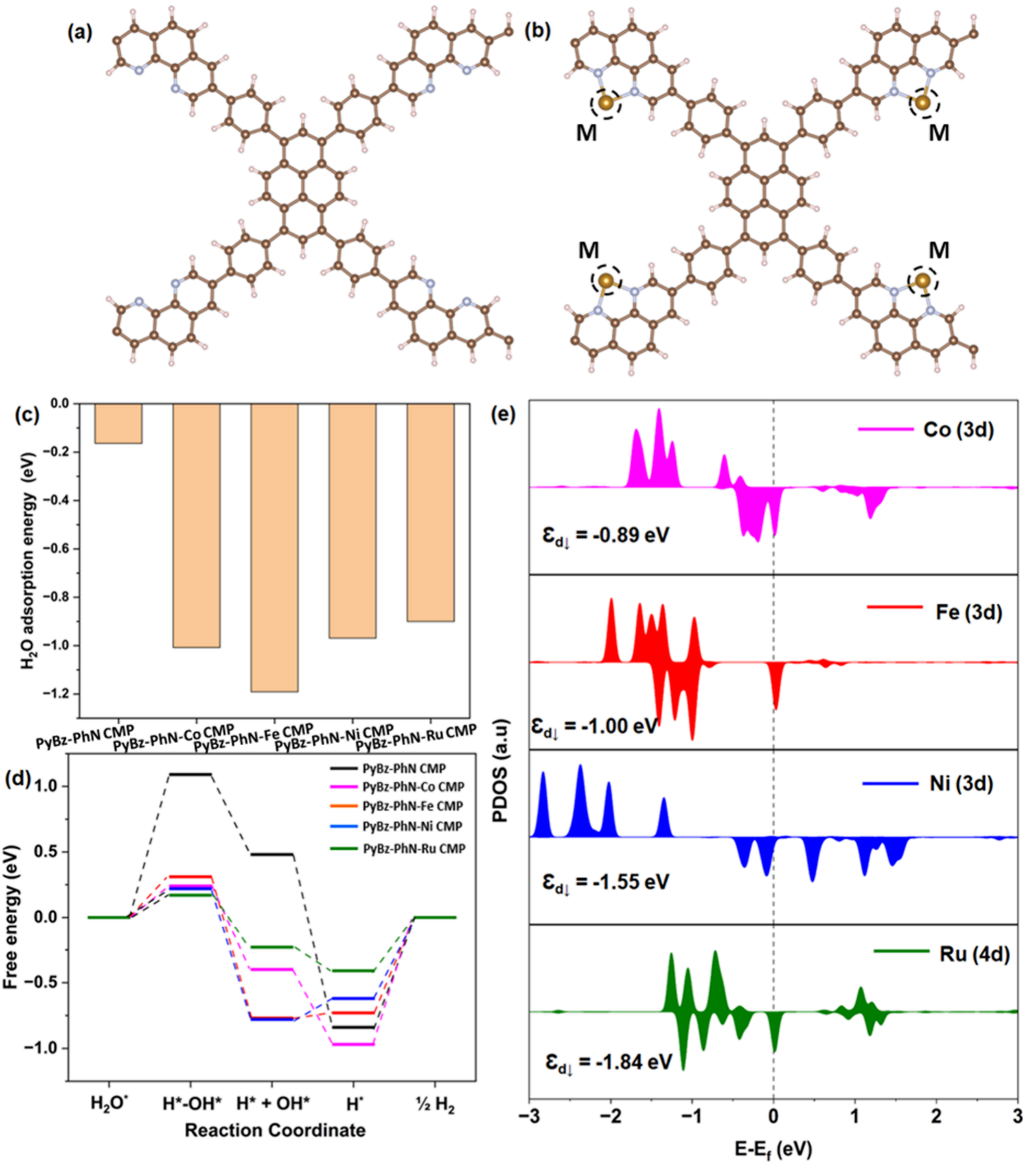

Figure 8. (a) Optimized configuration of pristine PyBz-PhN CMP, (b) PyBz-PhN-M CMPs (M = Fe^{2+}, Co^{2+}, Ni^{2+}, and Ru^{2+}), (c) adsorption energies of H_2O for various surfaces, (d) free energy diagram of HER (ΔG_{H*}) for various surfaces, and (e) PDOS of various Ms in PyBz-PhN-M CMPs.

CMP > PyBz-PhN CMP, which aligns well with the experimental results. These findings confirm that the improved HER activity of the PyBz-PhN-M CMPs series, particularly the Ru-based catalyst, stems from the reduced energy barriers and more favorable free energies associated with H_2O* and H* intermediates during the reaction process. To gain deeper insight into the electronic behavior of PyBz-PhN and PyBz-PhN-Ru CMPs during the water dissociation process, differential charge density (DCD) and Bader charge analyses were performed for the H_2O-adsorbed configurations. The DCD plots, presented in Figure S33, reveal distinct charge transfer from the metal atom to the adsorbed H_2O molecule. Quantitative Bader analysis indicates that approximately 0.073 e^- is transferred in the PyBz-PhN-Ru system, compared to only 0.028 e^- in the pristine PyBz-PhN. This enhanced electron transfer in PyBz-PhN-Ru weakens the O−H bond of the adsorbed H_2O molecule, resulting in a longer bond length of 0.977 Å. The elongation of the O−H bond signifies easier water dissociation, thereby facilitating the Volmer step during HER under alkaline conditions. The projected density of states (PDOS) plots for the various metal-coordinated CMPs are shown in Figure 8e. The pristine PyBz-PhN CMP exhibits a HOMO−LUMO gap of approximately 0.80 eV. Upon metal incorporation, additional metal d-states appear near the Fermi level, enhancing the density of available electronic states and promoting stronger interaction with HER intermediates. To further elucidate the hydrogen adsorption behavior, the d-band center (ε_d) relative to the Fermi level was calculated from the PDOS, as the binding strength of adsorbed hydrogen (H*) is intimately linked to the electronic structure of the active site.[66] A higher d-band ε_d value indicates more unoccupied antibonding states, typically resulting in stronger adsorption of reaction intermediates.[67] The spin-down d-band centers ($\varepsilon_{d\downarrow}$) for each metal-incorporated CMP are summarized in Figure 8e. Notably, a strong linear correlation between $\varepsilon_{d\downarrow}$ and ΔG_{H^*} (R^2 = 0.87) is observed, as shown in Figure S34, consistent with previous literature reports.[68] This correlation confirms that the *d*-band center is a key descriptor governing HER activity. Specifically, the upward shift of $\varepsilon_{d\downarrow}$ in PyBz-PhN-Co CMP accounts for its stronger H* adsorption, while the downward shift of $\varepsilon_{d\downarrow}$ in PyBz-PhN-Ru CMP weakens the H* adsorption to an optimal level. Such moderate binding strength is highly favorable for efficient HER kinetics, as it optimizes the adsorption and release of H* intermediates, thereby improving the overall hydrogen evolution activity.

■ CONCLUSIONS

In essence, we have demonstrated the successful fabrication of PyBz-PhN CMP and its metal-coordinated derivatives (PyBz-PhN-M CMPs; M = Fe^{2+}, Co^{2+}, Ni^{2+}, Ru^{2+}) via a one-pot Suzuki−Miyaura cross-coupling reaction. Comprehensive experimental investigations, combined with DFT calculations, confirm that metal coordination within the CMP framework significantly enhances catalytic activity for the HER. In particular, Ru incorporation effectively promotes key steps in the alkaline HER process, including water dissociation, H_2 adsorption, and H_2 generation, thereby improving overall reaction kinetics. As a result, PyBz-PhN-Ru CMP demonstrates notable electrocatalytic efficacy, exhibiting small overpotential requirements of 217 and 370 mV required to achieve 10 and 50 mA cm^{-2}, respectively. In addition, it exhibits a small Tafel slope of 127 mV dec^{-1}, a high C_{dl} of 0.206 mF, and a low R_{ct} of 89 Ω, confirming its superior HER activity compared with the other metal-coordinated analogues. Furthermore, enhanced HER behavior observed in Fe-, Co-, and Ni-modified CMPs, as opposed to PyBz-PhN CMP, underscores the critical role of metal coordination in tuning the electronic structure and optimizing catalytic properties. These results uncover critical aspects of the rational design of metal-coordinated CMPs as efficient and robust electrocatalysts for sustainable H_2 production.

■ ASSOCIATED CONTENT

Supporting Information

The Supporting Information is available free of charge at https://pubs.acs.org/doi/10.1021/acsaem.5c03684.

> Instrumentation, electrochemical measurements, computational methods, synthesis of PhN-2Br, FTIR and NMR data of PhN-2Br, XPS, UPS, and BET of PyBz-PhN CMP and PyBz-PhN-M CMPs, SEM, TEM, and TEM-EDS images of PyBz-PhN CMP and PyBz-PhN-M CMPs, LSV plots of PyBz-PhN-Ru CMP and Pt/C in 1.0 M KOH electrolyte, comparison bar charts of overpotentials at 100 mA cm^{-2} current densities of PyBz-PhN-M CMPs catalysts in alkaline electrolyte, Nyquist plots of PyBz-PhN CMP and PyBz-PhN-M CMPs catalysts in 1 M KOH medium at the overpotential of 200 Mv, CV profiles at different scan rates in the nonfaradaic region of PyBz-PhN CMP and PyBz-PhN-M CMPs, TOF comparison between synthesized PyBz-PhN CMP and PyBz-PhN-M CMPs at an overpotential of 450 mV in 1 M KOH solution, and chronoamperometry plot of PyBz-PhN-Ru CMP for 50 h in 1 M KOH (PDF)

■ AUTHOR INFORMATION

Corresponding Author

Shiao-Wei Kuo − *Department of Materials and Optoelectronic Science, Center for Functional Polymers and Supramolecular Materials, National Sun Yat-Sen University, Kaohsiung 804, Taiwan; Department of Medicinal and Applied Chemistry, Kaohsiung Medical University, Kaohsiung 807, Taiwan;* orcid.org/0000-0002-4306-7171; Email: kuosw@faculty.nsysu.edu.tw

Authors

Tapomay Mondal − *Department of Materials and Optoelectronic Science, Center for Functional Polymers and Supramolecular Materials, National Sun Yat-Sen University, Kaohsiung 804, Taiwan;* orcid.org/0009-0002-3355-9487

Mohamed Gamal Mohamed − *Department of Materials and Optoelectronic Science, Center for Functional Polymers and Supramolecular Materials, National Sun Yat-Sen University, Kaohsiung 804, Taiwan; Department of Chemistry, Faculty of Science, Assiut University, Assiut 71516, Egypt;* orcid.org/0000-0003-0301-8372

Muhammed Fasil Puthiyaparambath − *Department of Physics, SRM University-AP, Amaravati, Andhra Pradesh 522240, India*

Ranjit Thapa − *Department of Physics and Centre for Computational and Integrative Sciences, SRM University-AP, Amaravati, Andhra Pradesh 522240, India;* orcid.org/0000-0002-9285-0525

Complete contact information is available at:
https://pubs.acs.org/10.1021/acsaem.5c03684

Author Contributions

[#]T.M. and M.G.M. contributed equally to this work.

Notes

The authors declare no competing financial interest.

■ ACKNOWLEDGMENTS

This study was supported financially by the National Science and Technology Council, Taiwan, under contracts NSTC 114-2223-E-110-001- and 113-2221-E-110-012-MY3. The authors thank the staff at National Sun Yat-sen University for their assistance with the TEM (ID: EM022600) experiments. The authors thank the National Supercomputing Mission (NSM) for access to PARAM Rudra and PARAM Porul for computational work, and SRM University, Andhra Pradesh, India, for providing central computational facilities. M.F.P. and R.T. acknowledge ASEAN India Collaborative Research for the funding support CRD/2024/000716.

REFERENCES

(1) Prajapati, V.; Shah, A.; Patel, R.; Trivedi, N. A.; Som, N. N.; Srivastava, D. N.; Pataniya, P. M.; Sumesh, C. K. Utilizing electrooxidation for textile effluent wastewater treatment and simultaneous electrocatalytic hydrogen production: Transforming waste into energy and promoting water reuse in a circular economy context. *Renew. Energy* **2024**, *237*, No. 121733.

(2) Shah, A. M.; Modi, K. M.; Pataniya, P. M.; Joseph, K. S.; Dabhi, S.; Bhadu, G. R.; Sumesh, C. K. Self-Supported Mn-Ni_3Se_2 Electrocatalysts for Water and Urea Electrolysis for Energy-Saving Hydrogen Production. *ACS Appl. Mater. Interfaces* **2024**, *16*, 11440−11452.

(3) Thakkar, H. K.; Modi, K. H.; Joshi, K. K.; Bhadu, G.; Siraj, S.; Sahatiya, P.; Pataniya, P. M.; Sumesh, C. K. Vertically oriented FeNiO nanosheet array for urea and water electrolysis at industrial-scale current density. *ACS Sustainable Chem. Eng.* **2024**, *12*, 8340−8352.

(4) Patel, R. P.; Pataniya, P. M.; Patel, M.; Joshi, K.; Modi, K. H.; Sahatiya, P.; Sumesh, C. K. Hand-Print method for preparation of large area and binder free electrodes for photodetection and electrocatalytic hydrogen evolution. *Sol. Energy* **2022**, *246*, 343−354.

(5) Mohamed, M. G.; Elsayed, M. H.; Li, C. J.; Hassan, A. E.; Mekhemer, I. M. A.; Musa, A. F.; Hussien, M. K.; Chen, L. C.; Chen, K. H.; Chou, H. H.; Kuo, S. W. Reticular design and alkyne bridge engineering in donor−π−acceptor type conjugated microporous polymers for boosting photocatalytic hydrogen evolution. *J. Mater. Chem. A* **2024**, *12*, 7693−7710.

(6) Mohamed, M. G.; Mekhemer, I. M.; Selim, A. F.; Katsamitros, A.; Tasis, D.; Basit, A.; Chou, H.-H.; Kuo, S.-W. Molecular engineering of donor−acceptor-type conjugated microporous polymers for dual effective photocatalytic production of hydrogen and hydrogen peroxide. *Mater. Horiz.* **2025**, *12*, 5917−5928.

(7) Zhao, H.; Yuan, Z. Y. Progress and perspectives for solar-driven water electrolysis to produce green hydrogen. *Adv. Energy Mater.* **2023**, *13*, 2300254.

(8) Hoang, A. L.; Balakrishnan, S.; Hodges, A.; Tsekouras, G.; Al-Musawi, A.; Wagner, K.; Lee, C.-Y.; Swiegers, G. F.; Wallace, G. G. High-performing catalysts for energy-efficient commercial alkaline water electrolysis. *Sustain. Energy Fuels* **2022**, *7*, 31−60.

(9) Gao, G.; Zhu, G.; Chen, X.; Sun, Z.; Cabot, A. Optimizing Pt-based alloy electrocatalysts for improved hydrogen evolution performance in alkaline electrolytes: a comprehensive review. *ACS Nano* **2023**, *17*, 20804−20824.

(10) Zhang, Q.; Lao, M.; Yu, Y.; Ma, X.; Li, M.; Fei, Z.; Dyson, P. J.; Wang, S.; Min, D. Manipulation of the Electronic Structure of Ruthenium Nanoclusters by Ni-N_4 Sites Enhances the Alkaline Hydrogen Evolution Reaction. *Adv. Funct. Mater.* **2025**, *35*, 2416071.

(11) Zhang, X.; Guo, Y.; Wang, C. Multi-interface engineering of nickel-based electrocatalysts for alkaline hydrogen evolution reaction. *Energy Mater.* **2024**, *4*, 400044.

(12) Liu, Y.; Guo, Y.; Liu, Y.; Wei, Z.; Wang, K.; Shi, Z. A mini review on transition metal chalcogenides for electrocatalytic water splitting: bridging material design and practical application. *Energy Fuels* **2023**, *37*, 2608−2630.

(13) Dou, S.; Wang, X.; Wang, S. Rational design of transition metal-based materials for highly efficient electrocatalysis. *Small Methods* **2019**, *3*, 1800211.

(14) Huang, X.; Shen, T.; Zhang, T.; Qiu, H.; Gu, X.; Ali, Z.; Hou, Y. Efficient oxygen reduction catalysts of porous carbon nanostructures decorated with transition metal species. *Adv. Energy. Mater.* **2020**, *10*, 1900375.

(15) Banerjee, S.; Anayah, R. I.; Gerke, C. S.; Thoi, V. S. From molecules to porous materials: Integrating discrete electrocatalytic active sites into extended frameworks. *ACS Cent. Sci.* **2020**, *6*, 1671−1684.

(16) Mohamed, M. G.; Basit, A.; Shih, C.-Y.; Sharma, S. U.; Mondal, T.; Kuo, S.-W. Pyrene-Linked Covalent Organic Polymer/Single-Walled Carbon Nanotubes Hybrids as High-Performance Electrodes for Supercapacitive Energy Storage. *ACS Appl. Energy Mater.* **2025**, *8*, 3764−3778.

(17) Li, Y.; Wu, L.; Wang, K.; Zhou, B.; Li, Q.; Li, Z.; Yan, B.; Gong, C.; Wang, Q.; Jia, J.; Shen, H. M.; Deng, S.; Zhang, W.; She, Y. Nitrogen-rich conjugated microporous polymers with improved cobalt (II) density for highly efficient electrocatalytic oxygen evolution. *ACS Appl. Mater. Interfaces* **2024**, *16*, 8903−8912.

(18) Ye, Y. S.; Mohamed, M. G.; Ye, N. H.; Hung, T. Y.; Chen, G. Y.; Lin, S. H.; Tsai, M. C.; Hwang, B. J.; Kuo, S. W. Single-Atom Catalyst-Integrated Porous Organic Polymers for High-Performance Lithium-Sulfur Batteries. *Small* **2025**, *21*, 2503250.

(19) Wang, X.; Guo, A.; Fu, Y.; Tan, M.; Luo, W.; Yang, W. Porphyrin-conjugated microporous polymer nanospheres as electrocatalysts for nitrobenzene detection and oxygen evolution reaction. *ACS Appl. Nano Mater.* **2023**, *6*, 3226−3235.

(20) Mousa, A. O.; Sharma, S. U.; Chaganti, S. V.; Mansoure, T. H.; Singh, P. N.; Ejaz, M.; Chuang, C. H.; Lee, J. T.; Kuo, S. W.; Mohamed, M. G. Designing strategically functionalized conjugated microporous polymers with pyrene and perylenetetracarboxylic dianhydride moieties with single-walled carbon nanotubes to enhance supercapacitive energy storage efficiency. *J. Power Source* **2024**, *608*, No. 234624.

(21) Kotp, M. G.; Mohamed, M. G.; Kuo, S. W. Conjugated microporous polymer electrodes for supercapacitors: recent progress, key challenges, and future directions. *Chem. Sci.* **2025**, *16*, 20718−20754.

(22) Basit, A.; Mohamed, M. G.; Sharma, S. U.; Kuo, S.-W. Thianthrene-and thianthrene tetraoxide-functionalized conjugated microporous polymers for efficient energy storage. *ACS Appl. Polym. Mater.* **2024**, *6*, 12247−12260.

(23) Halder, B.; Mohamed, M. G.; Kalidoss, K.; Mohammed, A. A. K.; Singh, P. N.; Mondal, T.; Ye, Y.; Elumalai, P.; Kuo, S.-W. Synergistic bifunctional conjugated microporous polymer as an organic anode containing tetraphenylethene and thianthrene-5,5′,10,10′-tetraoxide units for lithium and sodium-ion batteries. *Mater. Adv.* **2025**, *6*, 5633−5647.

(24) Singh, P. N.; Mohamed, M. G.; Kotp, M. G.; Mondal, T.; Chaganti, S. V.; Ibrahim, M.; Sharma, S. U.; Ye, Y.; Kuo, S.-W. Nitrogen-and Sulfur-Rich Microporous Carbons Derived from Conjugated Microporous Polymers for CO_2 Uptake, Supercapacitor Energy Storage, and Electrochemical Hydrogen Production. *ACS Appl. Polym. Mater.* **2025**, *7*, 3324−3336.

(25) Mohamed, M. G.; Chen, C.-C.; Ibrahim, M.; Mousa, A. O.; Elsayed, M. H.; Ye, Y.; Kuo, S.-W. Tetraphenylanthraquinone and dihydroxybenzene-tethered conjugated microporous polymer for enhanced CO_2 uptake and supercapacitive energy storage. *JACS Au* **2024**, *4*, 3593−3605.

(26) Mohamed, M. G.; Kotp, M. G.; Mousa, A. O.; Li, Y. S.; Kuo, S. W. Construction of Fe-and N-Doped Microporous Carbon from Ferrocene-Based Conjugated Microporous Polymers for Supercapacitive Energy Storage. *ACS Appl. Energy Mater.* **2025**, *8*, 2389−2402.

(27) Mohamed, M. G.; Elewa, A. M.; Chen, N.-P.; Mohammed, A. A. K.; Kuo, S.-W. Construction of malononitrile-functionalized conjugated microporous polymers as adsorbents for effective adsorption of Rhodamine B and density functional theory perspective. *Coll. Surf. A: Physicochem. Eng. Asp.* **2025**, *721*, No. 137214.

(28) Mohamed, M. G.; Su, B.-X.; Kuo, S.-W. Robust nitrogen-doped microporous carbon via crown ether-functionalized benzoxazine-linked porous organic polymers for enhanced CO_2 adsorption and supercapacitor applications. *ACS Appl. Mater. Interfaces* **2024**, *16*, 40858−40872.

(29) Basit, A.; Kao, Y.-C.; El-Ossaily, Y. A.; Kuo, S.-W.; Mohamed, M. G. Rational engineering and synthesis of pyrene and thiazolo (5,4-d) thiazole-functionalized conjugated microporous polymers for

efficient supercapacitor energy storage. *J. Mater. Chem. A* **2024**, *12*, 30508−30521.

(30) Chung, W. T.; Mekhemer, I. M. A.; Mohamed, M. G.; Elewa, A. M.; EL-Mahdy, A. F. M.; Chou, H. H.; Kuo, S. W.; Wu, K. C. W. Recent advances in metal/covalent organic frameworks based materials: Their synthesis, structure design and potential applications for hydrogen production. *Coord. Chem. Rev.* **2023**, *483*, No. 215066.

(31) Ye, Y. S.; Mohamed, M. G.; Chen, W. C.; Kuo, S. W. Integrating the multiple functionalities in metalloporphyrin porous organic polymers enabling strong polysulfide anchoring and rapid electrochemical kinetics in Li−S batteries. *J. Mater. Chem. A* **2023**, *11*, 9112−9124.

(32) Guan, X.; Zhao, Y.; Pei, H.; Zhao, M.; Wang, Y.; Zhou, X.; Mohamed, M. G.; Kuo, S. W.; Ye, Y. Metalloporphyrin conjugated porous polymer in-situ grown on a Celgard separator as multifunctional polysulfide barrier and catalyst for high-performance Li-S batteries. *Chem. Eng. J.* **2023**, *473*, No. 144733.

(33) Mondal, T.; Mohamed, M. G.; Mohamed, A. A. K.; Kuo, S.-W. Construction of Metal-Coordinated Bipyridine-Based Conjugated Microporous Polymers as Robust Electrocatalysts for Hydrogen Evolution. *ACS Appl. Energy Mater.* **2025**, *8*, 7703−7713.

(34) Zhao, X.; Pachfule, P.; Li, S.; Langenhahn, T.; Ye, M.; Schlesiger, C.; Praetz, S.; Schmidt, J.; Thomas, A. Macro/microporous covalent organic frameworks for efficient electrocatalysis. *J. Am. Chem. Soc.* **2019**, *141*, 6623−6630.

(35) Pal, H.; Karmakar, A.; Sadhukhan, A.; Koner, K.; Karak, S.; Sharma, R. K.; Ghosh, M.; Dey, K. K.; Pathak, B.; Kundu, S.; Banerjee, R. Designing Salen-Based Porous Organic Polymers for Enhanced Electrolytic Water Splitting into Oxygen. *Adv. Funct. Mater.* **2024**, *34*, No. 2408255.

(36) Kao, Y. C.; Mondal, T.; Chang, W.-H.; Mohamed, M. G.; Kuo, S.-W. Structural tailoring of metal-coordinated salen-tetraphenylethene-based conjugated microporous polymers for superior active alkaline oxygen evolution electrocatalysis. *Int. J. Hydrogen Energy* **2025**, *173*, No. 151390.

(37) Lee, I. S.; Jeong, J. R.; Dang Van, C.; Lee, M. H. Transition metal−phenanthroline intercalated montmorillonite as efficient electrocatalysts for the oxygen evolution reaction. *J. Mater. Chem. A* **2025**, *13*, 13195−13204.

(38) Niu, T.; Yao, C.; Xie, W.; Zhang, S.; Xu, Y. A red luminescent Eu^{3+} doped conjugated microporous polymer for highly sensitive and selective detection of aluminum ions. *Polym. Chem.* **2021**, *12*, 356−360.

(39) Bansal, D.; Nada, A. A.; Ghosh, S.; Pandey, I. K.; Boscher, N. D. Porphyrin-based Polyimide 2D Porous Organic Polymers: Band Engineering for Bifunctional Electrocatalytic OER and HER. *Mater. Adv.* **2025**, *6*, 7932−7941.

(40) Das, S. K.; Chowdhury, A.; Bhunia, K.; Ghosh, A.; Chakraborty, D.; Das, M.; Kayal, U.; Modak, A.; Pradhan, D.; Bhaumik, A. Ni (II) and Cu (II) grafted porphyrin-pyrene based conjugated microporous polymers as bifunctional electrocatalysts for overall water splitting. *Electrochim. Acta* **2023**, *459*, No. 142553.

(41) Jia, H.; Yao, Y.; Gao, Y.; Lu, D.; Du, P. Pyrolyzed cobalt porphyrin-based conjugated mesoporous polymers as bifunctional catalysts for hydrogen production and oxygen evolution in water. *Chem. Commun.* **2016**, *52*, 13483−13486.

(42) Mohamed, M. G.; Chang, W.-C.; Kuo, S.-W. Crown ether-and benzoxazine-linked porous organic polymers displaying enhanced metal ion and CO$_2$ capture through solid-state chemical transformation. *Macromolecules* **2022**, *55*, 7879−7892.

(43) Mohamed, M. G.; Chen, T.-C.; Kuo, S.-W. Solid-state chemical transformations to enhance gas capture in benzoxazine-linked conjugated microporous polymers. *Macromolecules* **2021**, *54*, 5866−5877.

(44) Kao, Y.-C.; Mohamed, M. G.; Chen, Y.-H.; Ejaz, M.; Kuo, S.-W. Synergistic Engineering of Pyrene−Thiazolothiazole-Based Donor−π−Acceptor Conjugated Microporous Polymers with Heteroatom Embedding for Efficient Visible-Light Photocatalyst for Organic Dye Degradation. *ACS Polym. Au* **2025**, *5*, 633−644.

(45) Mohamed, M. G.; Halder, B.; Singh, P. N.; Mohammed, A. A. K.; Elumalai, P.; Kuo, S.-W. Molecular engineering and synergistic redox-active hexaazatrinaphthalene and pyrene-based conjugated microporous polymers for superior faradaic supercapacitor energy storage. *Chem. Eng. J.* **2025**, *520*, No. 165892.

(46) Mohamed, M. G.; Basit, A.; Madhu, M.; Aravinthkumar, K.; Said, A. I.; Manoj, D.; Tseng, W.-L.; Kuo, S.-W. Conjugated microporous polymer containing pyrene and dibenzo [g, p] chrysene moieties as a luminescent powerhouse for multi-target sensing and environmental safety. *Microporous Mesoporous Mater.* **2025**, *391*, No. 113620.

(47) Singh, S.; Ghorai, M. K.; Kar, K. K. A cobalt harnessed phenanthroline and triphenylamine-based conjugated mesoporous polymer designed by a donor−acceptor approach for trifunctional electrocatalysis. *J. Mater. Chem. A* **2023**, *11*, 20290−20301.

(48) Sarkar, S.; Dutta, T. K.; Mandal, B. P.; Patra, A. A porous organic polymer for symmetric sodium dual-ion batteries through an adsorption-intercalation-insertion mechanism. *Chem. Commun.* **2024**, *60*, 5010−5013.

(49) Han, J.; Zhu, Z.; Li, N.; Chen, D.; Xu, Q.; Li, H.; He, J.; Lu, J. Metalloporphyrin-based DA type conjugated organic polymer nanotube for efficient photocatalytic degradation. *Appl. Catal., B* **2021**, *291*, No. 120108.

(50) Chen, A.; Zhang, Y.; Chen, J.; Chen, L.; Yu, Y. Metalloporphyrin-based organic polymers for carbon dioxide fixation to cyclic carbonate. *J. Mater. Chem. A* **2015**, *3*, 9807−9816.

(51) Zong, L. P.; Li, J.; Shu, G.; Liu, X.; Marks, R. S.; Zhang, X. J.; Cosnier, S.; Shan, D. Rational design of a highly dispersed Fe−N−C nanosheet with 1, 10-phenanthroline-2, 9-dicarboxylic acid as a preorganized ligand: boosted electrochemiluminescence detection of tetracycline. *Anal. Chem.* **2021**, *94*, 1325−1332.

(52) Murugavel, R.; Korah, R. Structural diversity and supramolecular aggregation in calcium, strontium, and barium salicylates incorporating 1, 10-phenanthroline and 4, 4‘-bipyridine: probing the softer side of group 2 metal ions with pyridinic ligands. *Inorg. Chem.* **2007**, *46*, 11048−11062.

(53) Zhang, X.; Ding, J.; Qiu, B.; Li, D.; Bian, Y.; Zhu, D.; Wang, S.; Mai, W.; Ming, S.; Chen, J.; Li, T. Ultralow Co Loading Phenanthroline-based Porous Organic Polymer as a High-efficient Heterogeneous Catalyst for the Fixation of CO$_2$ to Cyclic Carbonates at Ambient Conditions. *ChemCatChem* **2021**, *13*, 2664−2673.

(54) Li, Y.; Liu, F.; Abdiryim, T.; Xu, F.; You, J.; Chen, J.; Yin, H.; Su, M.; Chen, L.; Jing, X.; Liu, X. Polyimide-based triazine-cored covalent organic frameworks supported metal (Fe, Ni, Ru and Rh) nanoparticles for high-efficiency electrocatalytic hydrogen evolution. *Int. J. Hydrogen Energy* **2024**, *94*, 53−62.

(55) Yang, S.; Yu, J.; Yao, C.; Li, S.; Xie, A. Preparation and electrocatalytic performance of N-doped hierarchical porous carbon loaded with Fe/Fe$_5$C$_2$ nanoparticles. *J. Alloys Compd.* **2022**, *903*, No. 163874.

(56) He, H.; Zhang, Q.; Li, S.; Wang, Z.; Zhao, J.; Luo, J.; Zhao, Y.; Zhang, X. Modulating metal activation energy via cerium-mediated heterointerface defect evolution for photovoltaic-driven efficient water electrolysis. *Nano Energy* **2025**, *134*, No. 110545.

(57) Liu, H.; Wei, G.; Xu, Z.; Liu, P.; Li, Y. Quantitative analysis of Fe and Co in Co-substituted magnetite using XPS: The application of non-linear least squares fitting (NLLSF). *Appl. Surf. Sci.* **2016**, *389*, 438−446.

(58) Whitten, J. E. Ultraviolet photoelectron spectroscopy: Practical aspects and best practices. *Appl. Surf. Sci. Adv.* **2023**, *13*, No. 100384.

(59) Song, W.; Chen, S.; Ren, X.; Su, X.; Song, C.; Li, Y.; Chen, L.; Bai, F. Isomeric Covalent Organic Frameworks for High-Efficiency Photocatalytic CO$_2$ Reduction: Substituent Position Effect. *Small* **2025**, *21*, 2409117.

(60) Zhang, B.; Chen, L.; Zhang, Z.; Li, Q.; Khangale, P.; Hildebrandt, D.; Liu, X.; Feng, Q.; Qiao, S. Modulating the band structure of metal coordinated salen COFs and an in situ constructed charge transfer heterostructure for electrocatalysis hydrogen evolution. *Adv. Sci.* **2022**, *9*, 2105912.

(61) Anantharaj, S. Hydrogen evolution reaction on Pt and Ru in alkali with volmer-step promotors and electronic structure modulators. *Curr. Opin. Electrochem.* **2022**, *33*, No. 100961.

(62) Charles, V.; Anumah, A. O.; Adegoke, K. A.; Adesina, M. O.; Ebuka, I. P.; Gaya, N. A.; Ogwuche, S.; Yakubu, M. O. Progress and challenges pertaining to the earthly-abundant electrocatalytic materials for oxygen evolution reaction. *Sus. Mater. Technol.* **2021**, *28*, No. e00252.

(63) Li, C.; Kim, B.; Li, Z.; Thapa, R.; Zhang, Y.; Seo, J. M.; Guan, R.; Tang, F.; Baek, J. H.; Kim, Y. H.; Jeon, J. P.; Park, N.; Baek, J. B. Direct Electroplating Ruthenium Precursor on the Surface Oxidized Nickel Foam for Efficient and Stable Bifunctional Alkaline Water Electrolysis. *Adv. Mater.* **2024**, *36*, 2403151.

(64) Yang, X.; Song, W.; Liao, K.; Wang, X.; Wang, X.; Zhang, J.; Wang, H.; Chen, Y.; Yan, N.; Han, X.; Ding, J.; Hu, W. Cohesive Energy Discrepancy Drives the Fabrication of Multimetallic Atomically Dispersed Materials for Hydrogen Evolution Reaction. *Nat. Commun.* **2024**, *15*, 8216.

(65) Cheng, F.; Peng, X.; Hu, L.; Yang, B.; Li, Z.; Dong, C. L.; Chen, J. L.; Hsu, L. C.; Lei, L.; Zheng, Q.; Qiu, M.; Dai, L.; Hou, Y. Accelerated Water Activation and Stabilized Metal-Organic Framework via Constructing Triangular Active-Regions for Ampere-Level Current Density Hydrogen Production. *Nat. Commun.* **2022**, *13*, 6486.

(66) Kou, T.; Chen, M.; Wu, F.; Smart, T. J.; Wang, S.; Wu, Y.; Zhang, Y.; Li, S.; Lall, S.; Zhang, Z.; Liu, Y. S.; Guo, J.; Wang, G.; Ping, Y.; Li, Y. Carbon Doping Switching on the Hydrogen Adsorption Activity of NiO for Hydrogen Evolution Reaction. *Nat. Commun.* **2020**, *11*, 590.

(67) Hammer, B.; Nørskov, J. K. Theoretical Surface Science and Catalysis-Calculations and Concepts. *Adv. Catal.* **2000**, *45*, 71−129.

(68) Wei, C.; Sun, Y.; Scherer, G. G.; Fisher, A. C.; Sherburne, M.; Ager, J. W.; Xu, Z. J. Surface Composition Dependent Ligand Effect in Tuning the Activity of Nickel−Copper Bimetallic Electrocatalysts toward Hydrogen Evolution in Alkaline. *J. Am. Chem. Soc.* **2020**, *142*, 7765−7775.